

# Generation and characterization of few-pulse attosecond pulse trains at 100 kHz repetition rate

Mikhail Osolodkov<sup>1</sup>, Federico J. Furch<sup>1</sup>, Felix Schell<sup>1</sup>, Peter Šušnjar<sup>1</sup>, Fabio Cavalcante<sup>2</sup>, Carmen S. Menoni<sup>2</sup>, Claus P. Schulz<sup>1</sup>, Tobias Witting<sup>1,\*</sup>, Marc J. J. Vrakking<sup>1</sup>

<sup>1</sup>Max Born Institute for Nonlinear Optics and Short Pulse Spectroscopy, Max-Born-Strasse 2a, 12489 Berlin, Germany

<sup>2</sup>Department of Electrical and Computer Engineering, Colorado State University, Fort Collins, CO 80523, USA

\*Corresponding author: tobias.witting@mbi-berlin.de

*Many experiments in attosecond science will benefit from attosecond pulses at high repetition rates with sufficient photon flux for pump-probe experiments. We use 7 fs, 800 nm pulses from a non-collinear optical parametric chirped pulse amplification (NOPCPA) laser system to generate few-pulse attosecond pulse trains (APTs) in the extreme ultraviolet (XUV) at a repetition rate of 100 kHz. The pulse trains have been fully characterized by recording FROG-CRAB (Frequency-Resolved Optical Gating for Complete Reconstruction of Attosecond Bursts) traces with a velocity map imaging spectrometer.*

Advances in the field of attosecond science are strongly related to advances of ultrashort laser sources. High energy near infrared (NIR) pulses with durations on the femtosecond timescale allow the generation of attosecond pulses in the extreme ultraviolet (XUV) through the process of high-order harmonic generation (HHG) [1]. Combined with phase-locked short NIR pulses in a pump-probe configuration, attosecond XUV pulses can be used for attosecond timescale spectroscopy experiments [2]. The process under investigation can be studied by measuring the absorption of the attosecond pulse or by detecting momentum distributions of photoelectrons or ions resulting from the interaction of the sample with a sequence of laser pulses. A more sophisticated approach than the latter is the coincidence detection of all charged particles following the interaction utilizing reaction microscopes or COLTRIMS (COLd Target Recoil Ion Momentum Spectroscopy) detectors [3]. Detection in coincidence allows measurement of the correlated three-dimensional momentum distributions of all charged particles resulting from the interaction. That information provides ac-

cess to the photoelectron momentum distributions in the recoil frame in the case of a dissociating molecule. Previously applied to strong field ionization experiments [4, 5], the coincidence detection technique has recently also been implemented for attosecond spectroscopy measurements. The combination of attosecond pump-probe spectroscopy with coincidence detection has made the spatio-temporal reconstruction of the photoionization process in a CO molecule [6] possible, and has been used to characterize the influence of electron-nuclear coupled dynamics on the phase of the entangled electron-nuclear wave packet during the dissociative ionization of H<sub>2</sub> molecules [7].

In order to perform coincidence detection measurements, a single ionization event restriction should be fulfilled, i.e. at most one ionized atom or molecule per laser shot. On the other hand, the number of detected events should be high enough to achieve good statistics. Together these two conditions result in the demand for high repetition rate laser systems with a sufficiently high pulse energy to generate XUV pulses. In recent years significant development of high repetition rate ( $\gg 10$  kHz) high en-

ergy laser sources enabled XUV generation at high repetition rates [8]. A number of groups have reported the generation of high-order harmonics at high repetition rate [9, 10, 11, 12]. So far, with the exception of [13, 14], who reported RABBITT experiments at 100 kHz using a fiber laser post-compressed to 40 fs, no pump-probe experiments or pulse characterization have been reported. In particular, there have not been any reports yet demonstrating the complete characterization of attosecond pulses generated using a high repetition rate, OPCPA driver, which is important given concerns that have existed in the past about spatio-temporal couplings in such systems [15, 16, 9]. In this Letter we report on the generation of few-pulse XUV attosecond pulse trains (APTs) in the 15 to 40 eV energy range with a flux of  $> 10^6$  photons per shot at a repetition rate of 100 kHz. We fully characterize the APTs using FROG-CRAB (Frequency-Resolved Optical Gating for Complete Reconstruction of Attosecond Bursts) [17]. The APTs are accompanied by phase-locked  $< 10$  fs NIR pulses for pump-probe experiments.

A sketch of the experimental setup is shown in Fig. 1. A noncollinear optical parametric chirped pulse amplification (NOPCPA) system is utilized as the drive laser for the experiment. It delivers up to 190  $\mu$ J, 7 fs pulses centered at 800 nm with a repetition rate of 100 kHz [18, 16]. The attosecond pump-probe setup consists of three separate interconnected vacuum chambers. In the *Splitting chamber* the NIR s-polarized pulses from the NOPCPA system are split into two beams with an 80/20 ratio using a beam splitter with a flat response over the spectral range 500-1100 nm. The majority (80%) of the incoming power is transmitted through the beam splitter and then used for the generation of high-order harmonics. In what follows we are going to refer to this arm of the interferometer as the *XUV arm* and to the other one as the *NIR arm*. In the *Splitting chamber* the high power NIR beam is focused by a spherical mirror ( $f = 50$  cm) into a 2 mm long gas cell positioned inside the *HHG chamber*. The NIR pulse compression is optimized for efficient high-order harmonic generation. The NIR peak intensity in the focus is on the order of 200 TW/cm<sup>2</sup>. After high-order harmonic

generation the high power NIR beam co-propagating with the XUV beam is filtered out in two steps in the *Recombination chamber*. First, the two-color beam is reflected by a specially designed dichroic mirror. The mirror has a Ta<sub>2</sub>O<sub>5</sub>/SiO<sub>2</sub> broadband antireflection coating for s- and p- polarization of the NIR beam topped by a 200 nm thick layer of SiO<sub>2</sub>. At a grazing incidence angle of 75 degrees the coating reflects the XUV beam with an average reflectivity of 45% in the 20-60 eV spectral range whereas only 20% of the NIR light is reflected, independent of the polarization. The rest of the NIR beam is transmitted by the filtering mirror and then sent to an external beam dump. In the second filtering step the remaining 20% of the NIR beam is blocked by a 200 nm thick aluminium filter mounted on a 1 mm thick fused silica plate. In the NIR arm of the interferometer, a translation stage with nanometer precision (SmarAct SLC-1750-S-HV) is used to control the delay between the pulses propagating in the two arms of the interferometer. A motorized iris (SmarAct SID-5714) installed in the NIR arm is used to control the NIR intensity delivered to the experiment by changing the size of the clear aperture. The beams from the XUV and NIR arms are recombined utilizing a recombination mirror shown schematically in the inset of Fig. 1. The recombination mirror has two 5 mm diameter drilled holes. They are oriented at 90 degrees with respect to each other and at 45 degrees to the mirror surface. The size of the clear aperture of the Al filter is the same as the size of the holes in the recombination mirror. The XUV beam transmitted through the Al filter propagates through one of the holes in the mirror. Part of the NIR beam from the NIR arm is reflected on the recombination mirror around the hole, resulting in an annular beam that is then recombined with the XUV beam and co-propagates towards the experiment. In the NIR arm we generate a focus in the equivalent plane to the HHG target. A gold-coated toroidal mirror forms a 1 : 1 image (object distance 1250 mm) of the two planes in the interaction region of the detection system, resulting in spatially overlapped foci of the XUV and NIR beams.

To enable attosecond pump-probe experiments the XUV- and NIR laser pulses from the pump-probe interferometer need to have a stable time-delay. We

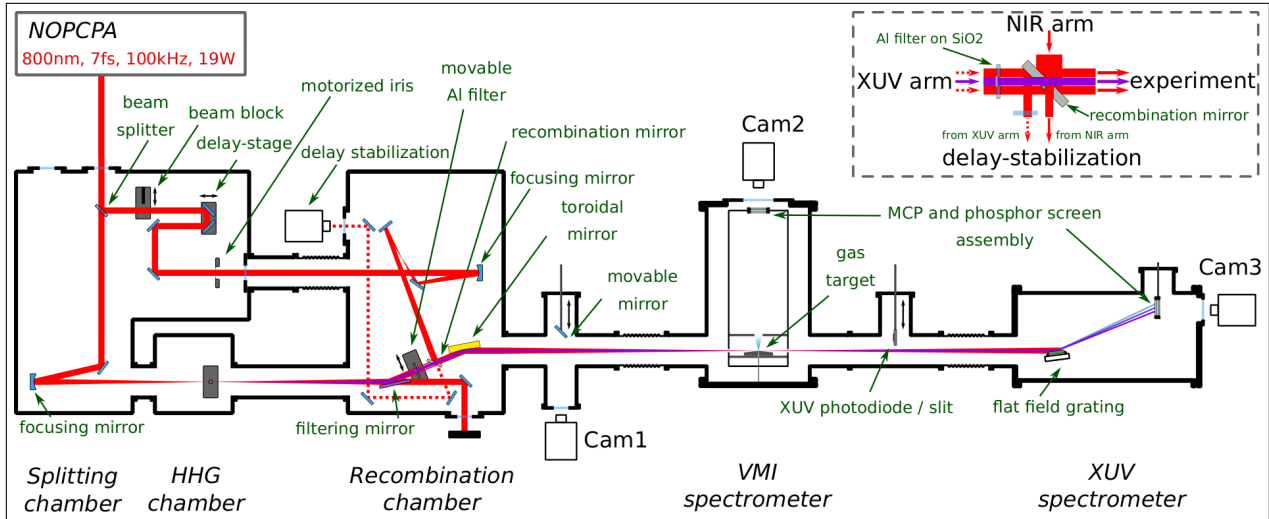


Figure 1: Schematic top view of the experimental setup. The NIR and XUV beams are shown in red and violet respectively. **Inset:** schematic view of the recombination mirror. For a detailed description please refer to the text.

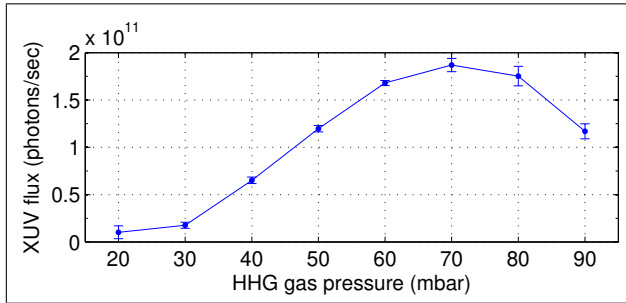


Figure 2: XUV photon flux on target as a function of the Kr pressure in the HHG target gas cell.

use a combination of passive and active stabilization schemes. The entire interferometer is built inside the vacuum system onto optical breadboards connected to an optical table and isolated from the chambers by bellows. The chambers are vibration-isolated from the optical table. For active stabilization we use the second output port of the recombination mirror. The beam layout is sketched in the inset of Fig. 1. We use the residual NIR from the XUV arm in combination with the transmitted NIR beam through the

recombination mirror. The central part of the beam from the NIR arm of the interferometer propagates through the second hole in the recombination mirror. Since the Al filter in the XUV arm is mounted on a fused silica plate and the size of the NIR beam incident on the Al-filter is larger than its diameter, the outer part of the beam is transmitted through the glass mount, while the central part is blocked by the filter. This annular beam is reflected by the back-side of the recombination mirror and then used together with the transmitted part of the NIR arm beam for delay-stabilization. We intentionally unbalance the glass amount in the two NIR beams (see inset Fig. 1) to introduce a time-delay of  $\approx 500$  fs. The resulting spectral interference fringes carry a  $\cos(\Delta\phi + \omega\tau)$  modulation and are recorded by a home-made spectrometer which is equipped with a fast USB 3 camera (Basler acA2040-90umNIR). The phase-shift is evaluated by a PC with a fast fourier transform (FFT)-based algorithm and a feedback signal is created controlling the delay-stage. Using a small region of interest on the camera chip we reach acquisition loop speeds of up to 1 kHz. However, we restrict the write speed to the piezo stage to  $< 250$  Hz to avoid reso-

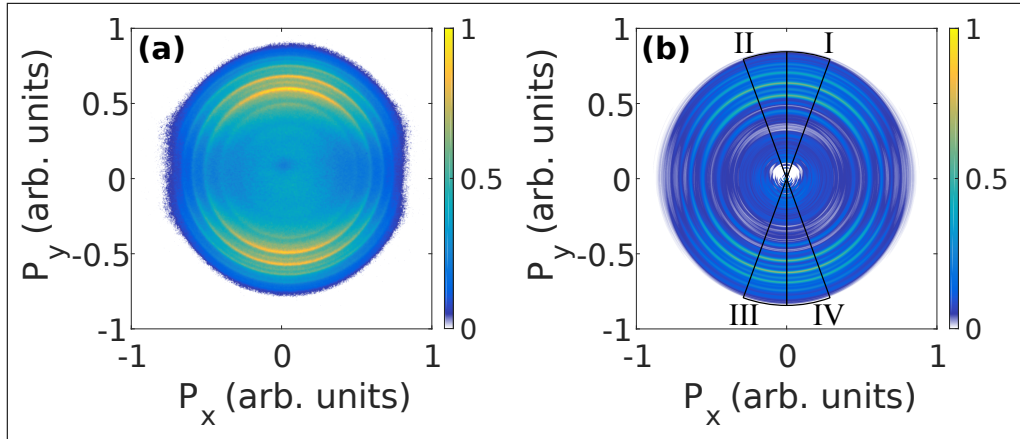


Figure 3: Two-color XUV+NIR VMI images with XUV and NIR pulses at temporal overlap. Raw data normalized to the maximum value (a), and a slice through the 3-dimensional retrieved momentum distribution (b). The NIR field-induced sidebands are visible along the laser polarization axis (parallel to  $p_y$ ). The four sections in (b) indicate the angular ranges used to create the four FROG-CRAB matrices employed for the four independent pulse reconstructions.

nances. This way pump-probe scans over 100s of fs can be performed with attosecond phase-lock. The delay stability is around 50 as rms over hours.

After the recombination chamber overlapping XUV and NIR pulses are focused onto a gas target in a velocity map imaging spectrometer (VMI). The sample atoms are ionized by the XUV beam and the resulting three dimensional photoelectron momentum distributions are projected onto a two-dimensional detector (micro channel plate (MCP) and phosphor screen assembly) by a set of two electrodes forming an electrostatic lens. A  $50 \mu\text{m}$  nozzle creating the gas target is incorporated into the repeller electrode in order to increase the gas density in the interaction region [19]. The signal on the MCP and phosphor screen assembly is recorded using a CMOS (complementary metaloxidesemiconductor) camera (Basler acA2040-90umNIR). An XUV spectrometer is positioned behind the VMI. It allows detection of the spatially resolved XUV spectrum during the experiment. The XUV spectrometer consists of a flat field grating (Hitachi) mounted on a motorized stage and an MCP and phosphor screen assembly detector. The signal on the detec-

tor is imaged by CCD (charge-coupled device) camera (BASLER scA1400-17gm) installed outside of the vacuum chamber.

In the present experiment high-order harmonics were generated in krypton gas. The XUV photon flux available for experiments was measured using an XUV photodiode (Opto diode AXUV100G) installed on a movable mount between the VMI and XUV spectrometer. The XUV photon flux as a function of the Kr pressure in the gas cell is shown in Fig. 2. The pump-probe measurements were performed with 70 mbar in the gas cell, which corresponds to an XUV photon flux of more than  $1.8 \times 10^{11}$  photons per second, or  $1.8 \times 10^6$  photons per shot in the interaction region of the experiment.

In the present pulse characterization experiment argon was used as a gas target. The Ar atoms were ionized by the XUV single photon absorption in the presence of a NIR field of intensity  $3 \text{ TW}/\text{cm}^2$ . Since the three-dimensional photoelectron momentum distributions have cylindrical symmetry along the laser polarization axis (along  $p_y$  in Fig. 3) they can be unambiguously retrieved from two-dimensional projections on a plane parallel to the axis of symmetry using

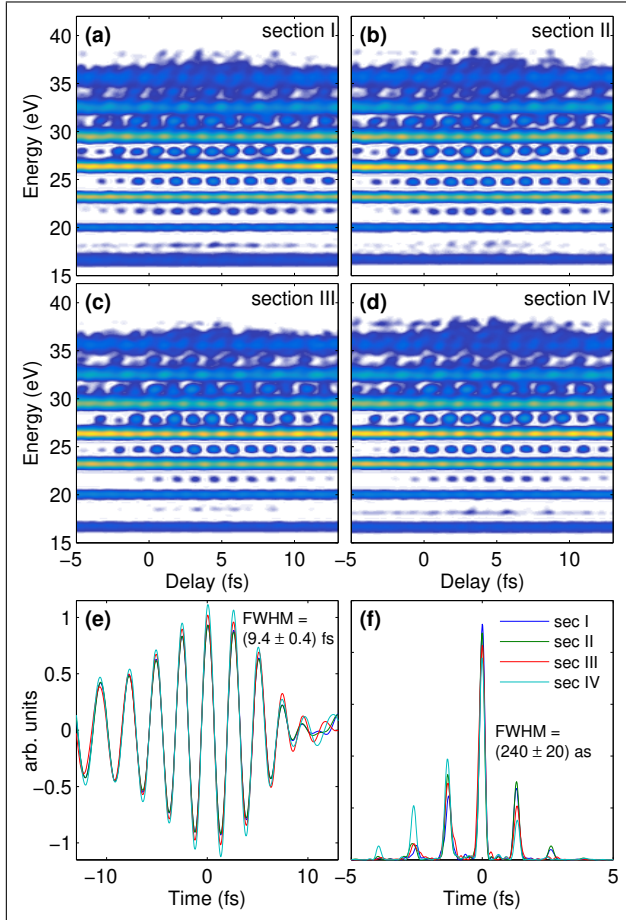


Figure 4: FROG-CRAB traces created by angular integration of areas I, II, III, and IV as indicated in Fig. 3(b) (a) to (d). Reconstructed NIR pulse electric fields (e) and reconstructed XUV attosecond pulse trains for each section (f).

an Abel inversion. Measured VMI images were inverted, using an inversion method based on fitting the measured projections of angular distributions in polar coordinates with Legendre polynomials [20]. VMI images were acquired for a pump-probe delay range of up to 40 fs with 100 as steps. The photoelectron momentum distributions were integrated over four different angle ranges of 20 degrees with respect to the laser polarization axis. The angular ranges of integration are shown as areas I, II, III and IV, in the retrieved three-dimensional momentum distribution in Fig. 3(b). Kinetic energy distributions were subsequently obtained by interpolating the integrated momentum distributions over an equally spaced kinetic energy axis.

In Figure 4(a) to (d) the resulting photoelectron kinetic energy distributions are plotted as a function of the delay between the NIR and XUV pulses. The energy axis is shown as photon energy, i.e. the ionization potential of argon (15.6 eV) is added to the energies of the detected photoelectrons. From the resulting photoelectron kinetic energy distributions as a function of the delay both the XUV and NIR pulses can be reconstructed. As our laser pulses of 7 fs generate APTs with only a few pulses, we are in a regime between long-pulse RABBITT where one can assume a periodic APT and streaking with isolated attosecond pulses. This manifests itself in the recorded FROG-CRAB traces (Fig. 4) as non-sidebandlike modulation especially around the higher energy harmonics. The structure and strength of the modulations are dependent on the NIR delay and therefore intensity, as opposed to regular same-strength modulations seen for a 10s of fs modulating pulse. Near the highest harmonics also the ‘harmonics’ are modulated in a streaking-like manner.

Therefore, a RABBITT-type analysis of fitting the sideband oscillations is not appropriate in our case. In order to retrieve the XUV and NIR pulses, we employ a time-domain ptychography algorithm [21, 22, 23]. This iterative algorithm enables the reconstruction of the complex electric fields of both, the unknown XUV, and the dressing NIR pulses. It was demonstrated to be more robust and converging faster than other well known reconstruction algorithms, such as the PCGPA (principal compo-

nent generalized projections algorithm) or LSGPA (least squares generalized projections algorithm) [22]. We run the time-domain ptychography algorithm in its extended ptychographic iterative engine (ePIE) implementation [22, 23] independently for the four traces from areas I, II, III, and IV. The time-delay axis was kept as acquired in the experiment with  $\delta\tau = 0.1$  fs and the photoelectron spectra were resampled onto a  $2^{12}$  pixel grid ( $\delta t = 20$  as,  $\delta\hbar\omega = 50$  meV). The ePIE algorithm retrieves the amplitudes and phases of the electron wavepacket from which we retrieve the complex electric field of the APT by subtracting the dipole transition phases [24]. The reconstructed NIR electric fields are shown in Fig. 4(e). The NIR pulses had an intensity FWHM duration of  $9.4 \pm 0.4$  fs. The pulse duration in the NIR arm is slightly longer than in the XUV arm, as the two arms are not perfectly dispersion-balanced. The 1 mm window between splitting and recombination chambers (see. Fig. 1) does not exactly compensate the dispersion of the 1 mm beamsplitter mounted at 45 deg. The reconstructed APTs (shown in Fig. 4(f)) consist of six individual attosecond pulses with one dominating main pulse. The duration of the central attosecond pulse is  $240 \pm 20$  as.

In conclusion, we have demonstrated the generation of attosecond pulse trains at 100 kHz repetition rate. We fully characterized the APTs using the FROG-CRAB scheme with a time-domain ptychography retrieval algorithm. Henceforth, the attosecond beamline reported here is going to be used for two-color XUV-NIR pump-probe spectroscopy measurements with coincidence detection in molecules.

**Funding.** European Union Horizon 2020 program Laserlab Europe (638585); European Union Horizon 2020 Marie Curie ITN project ASPIRE (674960). CSM acknowledges support of grant DoD ONR N00014-17-1-2536.

The authors thank R. Peslin, A. Loudovici, and Ch. Reiter for technical support.

## References

- [1] F. Krausz and M. Ivanov, **Reviews of Modern Physics** **81**, 163 (2009).
- [2] F. Lpine, M. Y. Ivanov, and M. J. J. Vrakking, **Nature Photonics** **8**, 195 (2014).
- [3] J. Ullrich, R. Moshhammer, A. Dorn, R. Dorn, L. Schmidt, and H. Schmidt-Bocking, **Reports on Progress in Physics** **66**, 1463 (2003).
- [4] B. Feuerstein, R. Moshhammer, D. Fischer, A. Dorn, C. Schrter, J. Deipenwisch, J. C. Lopez-Urrutia, C. Hhr, P. Neumayer, J. Ullrich, H. Rottke, C. Trump, M. Wittmann, G. Korn, , and W. Sandner, **Physical Review Letters** **87**, 043003 (2001).
- [5] E. Eremina, X. Liu, H. Rottke, W. Sandner, M. Schatzel, A. Dreischuh, G. Paulus, H. Walther, R. Moshhammer, and J. Ullrich, **Physical Review Letters** **92**, 173001 (2004).
- [6] J. Vos, L. Cattaneo, S. Patchkovskii, T. Zimmermann, C. Cirelli, M. Lucchini, A. Kheifets, A. S. Landsman, and U. Keller, **Science** **360**, 1326 (2018).
- [7] L. Cattaneo, J. Vos, R. Y. Bello, A. Palacios, S. Heuser, L. Pedrelli, M. Lucchini, C. Cirelli, F. Martn, and U. Keller, **Nature Physics** p. 1 (2018).
- [8] S. Hadrich, J. Rothhardt, M. Krebs, S. Demmier, A. Klenke, A. Tunnermann, and J. Limpert, **Journal of Physics B** **49**, 172002 (2016).
- [9] A. Harth, C. Guo, Y.-C. Cheng, A. Losquin, M. Miranda, S. Mikaelsson, C. M. Heyl, O. Prochnow, J. Ahrens, U. Morgner, A. L’Huillier, and C. L. Arnold, **Journal of Optics** **20**, 014007 (2017).
- [10] A. I. Gonzalez, G. Jargot, P. Rigaud, L. Lavenu, F. Guichard, A. Comby, T. Auguste, O. Sublemonties, M. Bougeard, Y. Zaouter, P. Georges, M. Hanna, and T. Ruchon, **Journal of the Optical Society of America B** **35**, A6 (2018).

- [11] E. Lorek, E. Larsen, C. Heyl, S. Carlstrom, D. Palecek, D. Zigmantas, and J. Mauritsson, **Review of Scientific Instruments** **85**, 123106 (2014).
- [12] M. Krebs, S. Hadrich, S. Demmler, J. Rothhardt, A. Zair, L. Chipperfield, J. Limpert, and A. Tunnermann, **Nature Photonics Letters** **7**, 555 (2013).
- [13] D. Hammerland, P. Zhang, S. Kuehn, P. Jojart, I. Seres, V. Zuba, Z. Varallyay, K. Osvay, T. T. Luu, and H. J. Woerner, **arXiv:1906.07059 [physics]** (2019). ArXiv: 1906.07059.
- [14] D. Hammerland, P. Zhang, A. Bray, C. F. Perry, S. Kuehn, P. Jojart, I. Seres, V. Zuba, Z. Varallyay, K. Osvay, A. Kheifets, T. T. Luu, and H. J. Woerner, **arXiv:1907.01219 [physics]** (2019). ArXiv: 1907.01219.
- [15] A. Giree, M. Mero, G. Arisholm, M. J. J. Vrakking, and F. J. Furch, **Optics Express** **25**, 3104 (2017).
- [16] T. Witting, F. J. Furch, and M. J. Vrakking, **Journal of Optics** **20**, 044003 (2018).
- [17] Y. Mairesse, , and F. Quere, **Physical Review A** **71**, 011401 (2005).
- [18] F. J. Furch, T. Witting, A. Giree, C. Luan, F. Schell, G. Arisholm, C. P. Schulz, and M. J. Vrakking, **Optics Letters** **42**, 2495 (2017).
- [19] O. Ghafur, W. Siu, P. Johnsson, M. F. Kling, M. Drescher, and M. J. Vrakking, **Review of Scientific Instruments** **80**, 033110 (2009).
- [20] G. Garcia, L. Nahon, and I. Powis, **Review of Scientific Instruments** **11**, 4989 (2004).
- [21] D. Spangenberg, E. Rohwer, M. H. Bruggemann, and T. Feurer, **Optics Letters** **40**, 1002 (2015).
- [22] M. Lucchini, M.H.Bruggemann, A. Ludwig, L. Gallmann, U. Keller, and T. Feurer, **Optics Express** **23**, 29502 (2015).
- [23] T. Witting, D. Greening, D. Walke, P. Matia-Hernando, T. Barillot, J. Marangos, and J. Tisch, **Optics Letters** **41**, 4218 (2016).
- [24] J. Mauritsson, M. B. Gaarde, and K. J. Schafer, **Physical Review A** **72**, 013401 (2005).